LAWRENCE
LIVERMORE
NATIONAL
LABORATORY

UCRL JRNL 202169

CODA-DERIVED SOURCE SPECTRA, MOMENT MAGNITUDES, AND ENERGY-MOMENT SCALING IN THE WESTERN ALPS

P. Morasca[1], K. Mayeda[2], L. Malagnini[3], and W. R. Walter[2]

[1]Universita' di Genova, [2]Lawrence Livermore National Laboratory, [3]Istituto Nazionale di Geofisica e Vulcanologia

Submitted to:
Geophysical Journal International

February 2004

DISCLAIMER

This work was performed under the auspices of the U.S. Department of Energy by the University of California, Lawrence Livermore National Laboratory under Contract No. W-7405-Eng-48.

CODA-DERIVED SOURCE SPECTRA, MOMENT MAGNITUDES, AND ENERGY-MOMENT SCALING IN THE WESTERN ALPS

P. Morasca (1), K. Mayeda (2), L. Malagnini (3), and William R. Walter(2)

(1) Universita' di Genova, (2) Lawrence Livermore National Laboratory, (3) Istituto Nazionale di Geofisica e Vulcanologia

alpocc@dipteris.unige.it, kmayeda@llnl.gov, malagnini@ingv.it, bwalter@llnl.gov

Abbreviated title: ENERGY-MOMENT SCALING IN THE WESTERN ALPS

Corresponding author: Paola Morasca
DipTeRis – Settore Geofisica
Universita' di Genova
Viale Benedetto XV, 5
16132 – Genova ITALY
e-mail: alpocc@dipteris.unige.it
Tel: 0039 – 010 – 3538343
Fax: 0039 – 010 - 3538081

In original form

SUMMARY

A stable estimate of the earthquake source spectra in the western Alps is obtained using an empirical method based on coda envelope amplitude measurements described by Mayeda *et al.* (2003) for events ranging between M_W~1.0 to ~5.0. We calibrated path corrections for consecutive narrow frequency bands ranging between 0.2 and 25.0-Hz using a simple 1-D model for 5 three-component stations of the Regional Seismic network of Northwestern Italy (RSNI). The 1-D assumption performs well, even though the region is characterized by a complex structural setting involving strong lateral variations in the Moho depth.

For frequencies less than 1.0-Hz, we tied our dimensionless, distance-corrected coda amplitudes to an absolute scale in units of dyne-cm by using independent moment magnitudes from long-period waveform modeling for 3 moderate magnitude events in the region. For the higher frequencies, we used small events as empirical Green's functions, with corner frequencies above 25.0-Hz. For each station, the procedure yields frequency-dependent corrections that account for site effects, including those related to f_{max}, as well as those related to *S*-to-coda transfer function effects. After the calibration was completed, the corrections were applied to the entire data-set composed of 957 events.

Our findings using the coda-derived source spectra are summarized as follows: (1) We derived stable estimates of seismic moment, M_0, (and hence M_W) as well as radiated *S*-wave energy, (E_S), from waveforms recorded by as few as one station, for events that were too small to be waveform modeled (i.e., events less than M_W ~3.5); (2) The source spectra were used to derive an equivalent local magnitude, $M_{L(coda)}$, that is in excellent agreement with the network averaged values using direct *S*-waves; (3) Scaled energy, $\tilde{e} = E_R/M_0$, where E_R, the radiated seismic energy, is comparable to results from other tectonically

active regions (e.g., western United States, Japan) and supports the idea that there is a fundamental difference in rupture dynamics between small and large crustal earthquakes in tectonically active regions.

Keywords: coda, energy, moment magnitude, source spectra, energy-moment scaling

INTRODUCTION

Virtually all source studies focus on the earthquake's direct phases such as *P*, *S*, or surface waves. The associated source parameters are inferred from spectral or waveform modeling usually adopting the omega-square source model (Brune, 1970; Aki, 1967). Direct wave amplitude measurements, however, are affected by source radiation pattern, directivity, and heterogeneities along the path, all of which can contribute to large amplitude variability (e.g., Favreau and Archuleta, 2002). Some recent studies that compare direct waves with coda waves (e.g., Mayeda, 1993; Mayeda and Walter, 1996; Mayeda *et al*., 2003; Eken *et al*., 2004; Malagnini *et al.,* 2004) find that amplitude measurements of direct waves requires significant multi-station averaging to achieve the same stability as a single coda envelope measurement, because the coda averages over path and source variability. In general, these studies find that the source amplitude obtained from the coda envelope is a factor of 3-to-4 times more stable than those derived from direct waves. In addition to source parameters such as focal mechanism and seismic moment release, there has been renewed interest in quantifying the dynamics of the earthquake rupture process over a broad range of event sizes (e.g., $1.0 < M_W < 8.0$). In the past, there were many studies that estimated the radiated energy for large magnitude events (e.g., Gutenberg and Richter, 1956; Vassiliou and Kanamori, 1982; Boatwright and Choy,

1986; Kikuchi and Fukao, 1988). More recently, with better instrumentation and denser networks, higher quality inversions for the rupture dynamics of large earthquakes (M_W > ~6.0) have been made (e.g., Kaverina *et al.*, 2002; Wald *et al.*, 1996; Kikuchi and Kanamori, 1991; Dreger *et al.*, 2003).

A source scaling study by Kanamori *et al*. (1993) observed an increasing trend in the energy-to-moment ratio, or scaled energy, $\tilde{e}$ (=E_R/M_0) with increasing M_0, which they interpreted as a difference in frictional behavior during rupture between small and large earthquakes (~3.5 < M_W < 7.2). However, difficulties exist in developing scaling relationships with small events because of limited resolution due to complex propagation in the crust and near surface attenuation that strongly affects the seismic waves at high frequency. Recently, Kanamori and Rivera (2004) discussed implications on rupture dynamics if the traditionally accepted static scaling relation (i.e., $M_0 \propto f_0^{-3}$) between M_0 and spectral corner frequency (f_0) is in fact scale-dependent. They showed that the dynamic scaling relation between E_R and M_0 and the static scaling relation are not independent. They point out the need to better constrain estimates of radiated energy (E_R), static stress drop ($\Delta\sigma_s$), and rupture speed (V) for small events in future studies. Estimating the radiated energy of smaller magnitude events (i.e., less than M_W ~3.5) requires integration of source spectra to very high frequencies. Unfortunately, surface stations, even under the best of circumstances (e.g., Steidl *et al.*, 1996), have significant near-site attenuation (e.g., site kappa, κ) and corrections must be applied, especially when considering small events where high frequencies are required. In the most severe cases, such as soft soil sites, there are simply no measurable signals at high frequency. To avoid the effects of near-surface attenuation, Abercrombie (1995) used high frequency recordings from the 2.5 km deep Cajon Pass borehole in Southern California, and a similar study was

performed in a 2 km borehole in Long Valley caldera in the eastern Sierra Nevada by Prejean and Ellsworth (2001). In both borehole studies, micro earthquake apparent stress was found to increase with moment, consistent with results of Kanamori *et al*. (1993) who considered much larger events.

Mayeda and Walter (1996) used a completely different approach using narrowband coda amplitude measurements to reconstruct the moment-rate spectra for continental crustal earthquakes distributed throughout the western United States (~3.0 < M_W < 7.2). Though they used broadband surface sensors, their methodology accounts for near-site attenuation and/or amplification effects. They found that $\tilde{e}$, and hence the apparent stress, increased as $M_0^{0.25}$ for events ranging between M_W 3.0 and 7.3. A similar scale-dependence in $\tilde{e}$ was also observed by Izutani and Kanamori (2001) for events in Japan.

Opposite conclusions have been obtained by Ide and Beroza (2001) and Pérez-Campos and Beroza (2001). In their study, they proposed that the different scaling purported between small and large earthquakes in other studies was due to improper computation of radiated energy at high frequency as well as to large scatter in the energy-moment ratio. It is clear that the existence of a scale-dependent energy-to-moment ratio is still in question because to obtain the source spectra, one must effectively remove all the propagation and site effects over a wide range of frequencies. In addition, earthquake sources are anisotropic and many of the larger events exhibit strong directivity thereby requiring good azimuthal averaging or *a priori* information to correct the amplitude spectra at a particular azimuth and distance from the source. For smaller events, where observations in $\tilde{e}$ are the most variable, the problem is compounded because small wavelength structures in the Earth are poorly resolved and may not be properly accounted for.

In the current study, we use the well-established coda stability to significantly reduce the measurement errors related to whole path propagation effects and random interference. We use a combination of larger calibration events with independent moments as well as empirical Green's function events to correct for *S*-to-coda transfer function effects and site response for frequencies ranging between 0.2 and 25.0-Hz.

STRUCTURAL SETTING

The region of the western Alps is laterally complicated and provides an excellent test of the coda method. In the following, we give a brief overview of the tectonics of the region. In the simplest form, the alpine chain is the result of northwest-southeast convergence between Africa and Europe (Polino *et al*., 1990; Giglia *et al*., 1996; Marchant and Stampfli, 1997; Rosenbaum *et al*., 2002). Usually researchers distinguish the western part of this chain in two belts (Sue *et al*., 1999; Eva *et al*., 1990): an external belt characterized by shallower earthquakes (<10 km) and an internal belt where events are located between 5 and 20 km (Paul *et al*., 2001). The Crustal Penninic Front (CPF) (Sue *et al*., 1999) is the main crustal discontinuity between the internal and external zones (see Fig. 1). From a geological viewpoint the area is characterized by crystalline massifs with a difference between the internal (Penninic) zone, showing high-grade metamorphic rocks, and the external zone that shows weakly deformed and metamorphosed rocks. As observed by Morasca *et al.* (2004), the region is characterized by a relatively low attenuation crustwhere $Q(f)=310f^{0.2}$. The relatively high *Q* of the western Alps indicates that the region may be considered more stable than, for example, the Apennines, where the circulating fluids and the regional heat flow are higher. However, this represents just a simplification because the tectonic processes that involve both the upper and lower crust is more complex,

as confirmed by anomalous structures such as the Ivrea body (Kissling, 1993; Di Stefano *et al*., 1999) and by the difficulties in defining the depth of the Moho beneath the region. In fact, the depth to the Moho in this area shows strong variations, ranging from 10 km in the Ligurian sea to a maximum of 50 km beneath the Alps (Buness *et al*., 1990).

The complex structure of the region has important implications in the western alpine tectonic regime, resulting in an inhomogeneous stress field (Sue *et al*., 1999) characterized by a radial shortening to the front of the belt and extension in the core (Eva and Solarino 1998; Sue and Tricart, 2002; Sue *et al*., 1999; Sue and Tricart, 1999). Such different tectonic regimes imply variations in ground motion levels, as suggested by many authors (Boore *et al*., 1997; Campell, 1997; Sadigh *et al*., 1997; Atkinson and Silva, 1997; Spudich *et al*., 1999; Atkinson and Boore, 1995).

DATA

In this study we analyzed over 900 earthquakes distributed throughout the western Alps (northwestern Italy) recorded by five, three-component, broadband sensors (Guralp CMG40), operated by the RSNI between 1996 and 2001 (see Fig. 1). Network-averaged local magnitudes (M_L) were computed for all the events by using a scale calibrated for northwestern Italy by Spallarossa *et al*. (2001). Our dataset consisted mainly of small events, $0.5 < M_L < 3.0$, and there were also a few greater than M_L 3, of which three were large enough to be waveform modeled. The hypocentral distance of the events ranged between 5 km and 160 km, with depths generally less than 15 km.

For the largest event, August 21st, 2000, (M_L 5.1), an M_W 4.8 was computed by MedNet (Istituto Nazionale di Geofisica e Vulcanologia, Italy). In addition, we performed 1-D waveform modeling for two other events, October 31st, 1997, (M_L 4.1) and April 11th,

1998, (M_L 3.6), using the methodology of Randall *et al.* (1995), obtaining M_W 4.11 and M_W 3.36, respectively. We used these three independent moment magnitudes as well as smaller events in order to calibrate and transform the non-dimensional, distance-corrected coda amplitudes into moment-rate spectra that are in units of dyne-cm.

METHOD

Overview

Mayeda and Walter (1996) used the seismic coda to minimize the effects of source radiation pattern, heterogeneous path effects, and near-site attenuation to produce stable estimates of moment-rate spectra, moment magnitude, and radiated seismic energy. They demonstrated that it is possible to produce extremely stable moment-rate spectra for regional earthquakes, even from single-station observations. For consecutive narrow frequency bands ranging between 0.02 and 8.0-Hz, they formed coda envelopes for each horizontal component using the equation:

$$E(t, f) = \sqrt{v(t)^2 + h(t)^2} \qquad (1)$$

where f is the center frequency, t is the time from the origin, $v(t)$ is the bandpass-filtered seismogram, and $h(t)$ is its corresponding Hilbert transform. They used the average of the two horizontal components, together with a 2-D theoretical multiple-scattering model (Shang and Gao, 1988) and produced synthetic coda envelopes as a function of time and epicentral distance. Calibrated synthetic envelopes were used to measure the observed envelope's amplitude as a function of frequency by DC shifting the synthetics until they matched the observed envelopes using an L-1 norm. In a recent study, Mayeda *et al.* (2003) improved upon this methodology and adopted a completely empirical approach for the computation of synthetic envelopes and path corrections applicable at both local and

regional distances. They argued that scattering theories to-date were still not sufficient to simultaneously predict the local and regional distance scattering using a single formulation. In fact, additional 'ad-hoc' distance corrections had to be used in the Mayeda and Walter (1996) study because the multiple-scattering model was too simplistic. In this paper we use the updated approach following Mayeda *et al*. (2003) where the coda amplitude at frequency f and distance r is written as:

$$A_c(f,t,r) = W_o(f)\cdot S(f)\cdot T(f)\cdot P(r,f)\cdot H\left(t-\frac{r}{v(r,f)}\right)\cdot\left(t-\frac{r}{v(r,f)}\right)^{-\gamma(r,f)}\cdot exp\left[b(r,f)\cdot\left(t-\frac{r}{v(r,f)}\right)\right] \quad (2)$$

where $W_o(f)$ is the *S*-wave source amplitude, $S(f)$ is the site response, $T(f)$ is the *S*-to-coda transfer function resulting from scattering conversion, $P(r,f)$ includes the effects of geometrical spreading and attenuation (both scattering and absorption), H is the Heaviside step function, $v(r,f)$ is the peak velocity of the *S*-wave arrival and $\gamma(r,f)$ and $b(r,f)$ control the coda envelope shape and t is the time in seconds from the origin time.

In this study, waveforms were narrowband-filtered in 14 consecutive frequency bands ranging between 0.2 and 25.0-Hz. For additional stability, we averaged the two horizontal envelopes then smoothed them using the methodology outlined in Mayeda *et al*. (2003). Figure 2 shows representative narrowband envelopes for the M_W 4.11 October 31st, 1997 event at station STV2.

Coda Shape and Velocity

The parameters, $v(r,f)$, $b(r,f)$ and $\gamma(r,f)$, were determined empirically for each station and then averaged over all 5 stations. For each narrow frequency band we describe $v(r,f)$, $b(r,f)$, and $\gamma(r,f)$,) by fitting the data with a simple form of a hyperbola as a function of distance r following Mayeda *et al.* (2003). For the group velocities of the envelope peak S arrival, $v(r)$, we used:

$$v(r) = v_0 - \frac{v_1}{v_2 + r} \qquad (3)$$

where v_0, v_1, and v_2, are the three parameters to describe the velocities as a function of distance that were determined through a simple grid-search. Likewise, for the envelope shape parameters, $b(r)$ and $\gamma(r)$, we used:

$$b(r) = b_0 - \frac{b_1}{b_2 + r} \qquad (4)$$

$$\gamma(r) = \gamma_0 - \frac{\gamma_1}{\gamma_2 + r} \qquad (5)$$

where b_0 ,b_1, b_2 and γ_0, γ_1, γ_2 were also obtained through a grid-search routine. We note that $\gamma(r,f)$ controls the shape of the early coda immediately following the direct waves, whereas $b(r,f)$ dominates the coda envelope shape at larger times well beyond the direct phase.

Figures 3a, 3b, and 3c show example data and best fitting curves for the three parameters $\gamma(r,f)$, $b(r,f)$, and $v(r,f)$ for the 4.0-6.0-Hz band. In general, most of the data in this study could be fit with a line, but for flexibility and consistency with past studies, we are using the form of a hyperbola. Once $\gamma(r,f)$, $b(r,f)$, and $v(r,f)$ are obtained, synthetic envelopes can be formed and used to measure each observed, narrowband envelope (see Mayeda *et al.*, 2003). Table 1 lists best fitting average parameters for each narrow frequency band.

Synthetic Envelopes

As for measuring the coda envelope amplitude, we modified our procedure from that of Mayeda *et al*. (2003) by normalizing the synthetics at a fixed lapse time (120 seconds) as measured from the origin time. This normalization procedure has no effect on the final coda-derived source spectra, however it makes the interpretation of our path attenuation parameters more consistent with local and regional coda observations. Specifically, observations of local coda energy appear to be homogeneously distributed in time and space behind the expanding direct wave front (e.g., see review by Sato and Fehler, 1998). To illustrate this, Figures 4a and 4b show coda envelopes for two events recorded at stations STV2 and NEGI for two narrow frequency bands (e.g., 2.0-3.0-Hz and 20.0-25.0-Hz). For both events, independent of distance from either station, we see that the coda envelopes attain roughly the same level and shape, whereas their corresponding direct *S*-waves decrease rapidly as a function of distance due to geometrical spreading and attenuation. For the 2.0-3.0-Hz case we note that the early coda immediately following the direct *S*-wave for the closer recordings are steep relative to the more distant recordings, but this is accounted for by having a distance-dependent γ. To generate the synthetics, we first set *W, S,* and *T* to unity in Equation 2, then normalized each synthetic to 120 seconds past the origin time. Figure 4c shows normalized synthetics for the 2.0-3.0-Hz case generated at 20 km intervals, ranging between 20 and 200 km and Figure 4d is for the 20.0-25.0-Hz case. The character of these synthetics are consistent with what we observe in Figures 4a and 4b which exhibit steep early coda at short distances, but similar shapes and levels at larger lapse times and distances.

Amplitude Measurements and Path Correction

For each observed envelope we measured its relative amplitude by vertically DC shifting the normalized synthetic envelope to match the observed envelope using an L-1 fit. For multiple pairs of stations, we selected common events that had good signal-to-noise ratio at both stations (calibration events) and performed a grid-search based on a relation that was used previously by Mayeda *et al*. (2003) for Dead Sea rift earthquakes:

$$P(r,f) = \left[1 + \left(\frac{r}{p_2}\right)^{p_1}\right]^{-1} \qquad (6)$$

where f is the center frequency, r the epicentral distance and p_1, p_2 are the path parameters from the grid-search for each frequency band. The path correction P is approximately constant for values of r less than p_2 whereas for values of $r \gg p_2$, it decays proportionally to the p_1 power. The parameter p_2 can be interpreted as the critical distance beyond which the coda is no longer homogeneously distributed in space and the parameter p_1 controls how rapidly the coda envelope level decreases with increasing distance.

Other empirical functions could be used, but the functional form of Equation 6 appears to be perfectly adequate and agrees well with local and regional coda observations throughout the world (e.g., Sato and Fehler, 1998). In general, a correction function could be determined for each station, but we have assumed the simplest case of a laterally homogeneous region, therefore requiring that the two parameters be the same for all stations, for each frequency band. For each frequency band the parameters p_1 and p_2 were chosen based on the lowest average inter-station standard deviation (see Table 1). Figure 5 shows examples of direct *S* and coda waves before and after distance corrections were applied. For the correction of direct *S*-waves, we used a path correction according to Morasca *et al.* (2004), who determined attenuation specific to this region. For nearly all

frequency bands, the coda inter-station data standard deviation is usually below 0.1 whereas the direct *S*-wave scatter is a factor of 3-to-4 larger, consistent with past coda studies. We note that the "raw" or uncorrected coda amplitudes have very small interstation scatter. This is because our initial normalized synthetics are a very good first approximation to the actual coda attenuation. Had we not normalized our synthetics first, this would have severely increased the scatter, comparable to those of the direct waves. Finally, the constant shift of the data points observed in Figure 5 with respect to the line y=x, represents the relative site effect for the specific station pair, at the specific frequency (e.g., see also Figure 6 of Mayeda and Walter, 1996).

Transformation to Moment-Rate Spectra

Figure 6a shows distance-corrected coda spectra in dimensionless units for our three calibration events along with two smaller events that we are using as empirical Green's functions. In order to transform these spectra into an absolute scale, we need to correct for frequency-dependent *S*-to-coda transfer functions and site effects, which we call "site-transfer" corrections. Following Mayeda and Walter (1996) and Mayeda *et al.* (2003), we tie the lower frequencies to independent moments determined from long-period waveform modeling. Figure 6b shows an example of 1-D waveform modeling for one of the calibration earthquakes and the corresponding seismic moment. Assuming that the smallest of our calibration events (April 11th, 1998, M_W 3.36), has a corner frequency above 1-Hz, we can find the frequency-dependent corrections that, in a least squares sense, match our three independent moments, thereby giving us the corrections between $0.2 \leq f \leq 1.0$-Hz that we will use for all events in that frequency band. For frequencies above 1-Hz we use small events as empirical Green's functions noting that these events are around $1.0 \leq M_W \leq 1.6$

based upon their corrected 1-Hz amplitudes. Next, assuming that these small events have flat source spectra at least up to ~25.0-Hz, we flatten each spectrum to be consistent with its previously corrected lower frequency amplitude at 1-Hz. Since we use many Green's function events (not just the two shown in Figure 6a), we obtain the average correction for each station for $1.0 < f \leq 25.0$-Hz. This assumption is consistent with high-quality source spectra observed by Abercrombie (1995) and Prejean and Ellsworth (2001) for comparable sized events from their respective borehole studies. Finally, Figure 6c shows the transformation of the non-dimensional spectra in Figure 6a to absolute source spectra that are now in units of dyne-cm. To reiterate, this procedure accounts for all frequency-dependent path, *S*-to-coda transfer function, and site effects. These corrections are then applied to the entire dataset to form source moment-rate spectra, then consequently used to estimate seismic moment and radiated *S*-wave energy. The frequency-dependent site-transfer corrections for each station are listed in Table 2.

RESULTS

Magnitudes

After applying the path and site-transfer corrections to all the data we computed averaged source spectra for additional stability. For each averaged source spectrum, we averaged the amplitudes of the two lowest frequencies to estimate the seismic moment, and the moment magnitude, $M_{W(coda)}$, was computed using the relation, $M_W = 2/3 \log_{10} M_0 - 10.73$ by Hanks and Kanamori (1979). Figure 7a shows good agreement between $M_{W(coda)}$ and M_W derived by Morasca *et al.* (2004) using direct waves. Next, we compared the coda-derived M_W's against the network-averaged M_L's that were defined using a local magnitude

scale calibrated for northwestern Italy by Spallarossa *et al*. (2002) (Fig. 7b). From Figure 7b, we see that $M_{W(coda)}$ scales with a 2/3 slope for small events (i.e., M_L less then ~3) and scales roughly 1-to-1 for the intermediate magnitude events. This scaling is expected based upon the definition of Kanamori (1977), because M_W is proportional to 2/3 $\log_{10}M_0$ whereas M_L is proportional to log amplitude. Finally, to obtain a stable equivalent M_L, we regressed the 2.0-3.0-Hz source spectral amplitudes with the network M_L and found the following relation,

$$M_{L(coda)} = \left(\log_{10} A_c - 17.5\right) \Big/ 0.93 \qquad (7)$$

where A_c is the coda-derived source amplitude at 2.0-3.0-Hz in dyne-cm. We see from Figure 7c that we have good agreement with the network results with the added advantage that a stable estimate of $M_{L(coda)}$ can be obtained from as few as one station as opposed to the traditional M_L which requires network averaging to reduce scatter.

Radiated Energy

We now focus our attention on quantifying the dynamic stress drop scaling in the region by computing the radiated *S*-wave energy (E_S) from the observed source spectra. As previously done by Mayeda and Walter (1996), we extrapolated the observed coda-derived moment-rate spectra, $\dot{M}(\omega)$, to both high (f=∞-Hz) and low frequency (f=0-Hz) limits, converted to velocity by multiplying by omega ($\omega=2\pi f$), squared the spectra and then integrated to obtain E_S. Assuming that the *P*-wave contribution is 7% of the total radiated elastic wave energy, we multiplied E_S by 1.07 to obtain the total radiated energy, where E_S is,

$$E_s = \frac{I}{4\pi^2 \rho \beta^5} \int_0^\infty \left| \omega \cdot \dot{M}(\omega) \right|^2 d\omega \qquad (8)$$

where the RMS radiation pattern for *S*-waves $I = 2/5$, the density $\rho = 2700$ kg/m^3, and the *S*-wave velocity β=3.5 km/s.

Figure 8 shows the western Alps energy estimates for two subsets of data compared against previous results from the western United States. The first are events where we extrapolated less than 30% of the total *S*-wave energy and the other set are events where we extrapolated between 30-to-45%. In all cases, the energy extrapolated at the low frequencies (f=0-Hz) is minimal, contributing less than a few percent. Even for the second set of events, where the extrapolation was the largest, all of these events had observed corner frequencies. In contrast, smaller events ($M_W < 2.0$) such as those used as empirical Green's functions had flat source spectra at least up to 25.0-Hz (e.g., see Fig. 6c) and were not used in the energy estimation. From Figure 8 we see that both subsets of data generally follow the scaling that was previously observed in the western United States by Mayeda *et al.* (1996) and is in good agreement with those from the Cajon Pass borehole study of Abercrombie (1995). For the larger events ($M_W > 3.5$) there appears to be evidence for slightly elevated apparent stress (> 3 MPa) which might reflect differences in the state of stress in this region. This same elevated level is also observed for comparable sized earthquakes in the Sierra Nevada batholith, when compared against earthquakes distributed throughout northern California (Mayeda *et al*., 2004).

Our results show that with good, high frequency data and the proper corrections for attenuation and site effect, it is possible to obtain stable energy estimates for events with

M_W ~2.5 or larger using surface sensors. This assertion is supported by borehole studies which also observe *S*-wave corner frequencies between ~10 and 20-Hz for events near M_W 2.5 (e.g., Abercrombie, 1995; Prejean and Ellsworth, 2001). For this reason, we cannot make reliable energy estimates below ~ M_W 2.5 for this dataset, however for events above this there is clearly an increasing trend in scaled energy, $\tilde{e}$, with increasing moment.

DISCUSSION

We successfully transported the coda methodology to the region of the western Alps, measured stable, absolute source parameters such as E_S and M_0 and derived band-limited magnitudes such as M_L from as few as one station. We believe that application of the coda methodology to the western Alps dataset overcomes the difficulties associated with properly accounting for high frequency attenuation and site response. Our moment-rate spectra appear to be free of source radiation pattern and virtually insensitive to lateral crustal heterogeneity. Our coda-derived estimates of M_L and M_W are in excellent agreement with network-averaged results but are significantly more stable. In addition, we examined the dynamic stress drop scaling in the region by computing the radiated *S*-wave energy (E_S) from the source spectra of events M_W ~2.5 and larger. We showed that the scaled energy, $\tilde{e}$, and hence the dynamic stress-drop, or "apparent stress" (e.g., Aki, 1966; Wyss and Brune, 1968) is not constant in this region and increases with increasing seismic moment, in good agreement with results from the western United States (e.g., Kanamori *et al*., 1993; Abercrombie, 1995; Mayeda and Walter, 1996, Prejean and Ellsworth, 2001) and Japan (Izutani and Kanamori, 2001). We note that the apparent stress for the moderate sized events is systematically larger by a factor of 2 than those from the western United States which might reflect a higher state of stress in the current study region.

Although Ide and Beroza (2001) suggested that the reported scaling of radiated energy of small events may be due to band limitations, considering events for which we observed at least 55% of total radiated *S*-wave energy, we do observe a difference in $\tilde{e}$ for events above M_W ~2.5. As Kanamori and Heaton (2000) argue, we also believe that even if we allow for deficiency in energy estimates, the stress drop variation is too significant to be discounted. Attenuation and propagation effects may introduce errors in energy estimates (Ide and Beroza 2001, Izutani and Kanamori 2001) but we feel confident that we accounted for all frequency-dependent path attenuation and site effects by a careful empirical calibration analysis that yielded stable source spectra. Our results support the idea that differences exist between the dynamics of small and large earthquakes (Kanamori and Heaton 2000, Izutani and Kanamori 2001, Brodsky and Kanamori 2001). Various mechanisms are suggested to justify the relative increase of radiated energy with earthquake size. Non-linear processes such as fault melting or thermal fluidization can lower the dynamic frictional stress for large slip, causing a production of a larger amount of radiated seismic energy (Kanamori and Heaton, 2000). The elasto-dynamic theory proposed by Brodsky and Kanamori (2001) argues that there is a reduction in friction for large events relative to small events independent of any thermal effects. They contend that the presence of fluids in a fault under certain circumstances can produce a viscous stress balanced by dynamic pressure that reduces friction. Another interesting possibility is that large earthquakes tend to occur on well-developed mature faults, so that the fracture energy could be very small. For small earthquakes the fracture energy is relatively large, because they often occur on smaller cracks that need a lot of energy to grow (Kanamori and Brodsky, 2001). We believe that our stable results focusing on small earthquakes can be a

useful contribution to highlight the way earthquake radiated energy scales with increasing magnitude.

ACKNOWLEDGMENTS

The authors wish to thank Prof. Claudio Eva and the RSNI network staff (G. Carenzo, M.Pasta and E. Zunino) for the careful network management and data collection that made this work possible. We are also indebted to the reviewers, N. Deichmann and K. Koch that provided valuable comments that significantly improved the original manuscript. Dr. Mayeda's work was performed under the auspices of the U.S. Department of Energy by the University of California, Lawrence Livermore National Laboratory under contract No. W-7405-Eng-48. This is LLNL contribution UCRL-JRNL-xxxxxx.

REFERENCES

Abercrombie, R. E., Earthquake source scaling relationship from 1 to 5 ML using seismograms recorded at 2.5 Km depth. *J. Geophys. Res.* **100**, 24,015-24,036, 1995.

Aki, K., Generation and propagation of G waves from the Niigata earthquake of June 16, 1964. Part 2. Estimation of earthquake moment from the G wave spectrum. *Bull. Earthquake Res. Inst. Tokio Univ.* **44**, 73-88, 1966.

Aki, K., Scaling law of seismic spectrum. *J. Geophys. Res.* **72**, 1217-1231, 1967.

Atkinson, G. M., and D. M., Boore . Ground Motion Relations for Eastern North America. *Bull. Seism. Soc. Am.,* **85**, n 1, 17-30, 1995.

Atkinson, G. M. and W. J. Silva An empirical study on earthquake source spectra. *Bull. Seism. Soc. Am.,* **87**, 97-113, 1997.

Boatwright, J. and Choy, G. L., Teleseismic estimates of the energy radiated by shallow earthquakes. *U. S. Geol. Surv. Open file Rept. 85-0290-A. Workshop XXVIII on the Borah Peak, Idaho earthquake edited by R. S. Stein, R. C. Bucknam, M. L. Jacobson* 409-448, 1986.

Boore, D. M., Joyner, W. B., Fumal, E. T. Equations for estimating horizontal response spectra and peak acceleration from western North American earthquakes: A summary of recent work, *Seism. Res. Lett.,* **68**, 1, 129-154, 1997.

Brodsky E. E. and Kanamori H., Elastohydrodynamic lubrification of faults, *J. Geophys. Res.* **106**, B8, 16,357-16,374, 2001.

Brune, J. N. Tectonic stress and spectra of seismic shear waves from earthquakes, *J. Geophys. Res.* **75**, 4997-5009, 1970.

Buness, H., Giese, P., Hirn, A., Nadir, S., Scarascia, S., Crustal structure derived from

seismic refraction between Southern Alps and the Ligurian Sea. *Proceeding of the Sixth Workshop on the EGT Project: data compilation and synoptic interpretation, edited by R. Freeman and St. Mueller (European Science Foundation, Strasbourg, France),*165-167, 1990.

Campell, W. K. Empirical near-source attenuation relationships for horizontal and vertical components of peak ground acceleration, peak ground velocity, and pseudo-absolute acceleration response spectra, *Seism. Res. Lett*., **68**, 1, 128-154, 1997.

Di Stefano, R., Chiarabba, C., Lucente, F. and A., Amato. Crustal and uppermost mantle structure in Italy from the inversion of P-wave arrival times: geodynamic implications. *Geophys. J. Int.* **139**, 483-498, 1999.

Dreger, D. S., D. Oglesby, R. Harris, N. Ratchkovski, and R. Hansen, Kinematic and dynamic rupture models of the November 3, 2002 M_w7.9 Denali, Alaska earthquake, submitted to *Geophys. Res. Lett*., 2003.

Eken, T., K. Mayeda, A. Hofstetter, R. Gök, G. Örgülü and N. Turkelli, An application of the coda methodology for moment-rate spectra using broadband stations in Turkey, *Geophys. Res. Lett*. **31**, ????, 2004.

Eva, C., Augliera, P., Cattaneo, M., Pastore, S., Tommaselli, A., Sismotettonica dell'Italia Nord-Occidentale. *Atti del Convegno GNDT,* vol. 1, pp. 35-51, 1990.

Eva, E. and Solarino, S., Variations of stress directions in the western Alpine arc. *Geophys. J. Int.* **135**,438-448. 1998.

Favreau, P. and R. J. Archuleta, Direct seismic energy modeling and application to the 1979 Imperial Valley earthquake, *Geophys. Res. Lett*. 30, 1198, 2003.

Giglia, G., Capponi, G., Crispini, L., Piazza, M., Dynamics and seismotectonics of the West-Alpine arc. *Tectonophysics* **267**, 143-175, 1996.

Guttenberg, B., and C. F. Richter, Magnitude and energy of earthquakes, Ann. Geofis. **9**, 1-15, 1956.

Ide, S and Beroza, G. C., Does apparent stress vary with earthquake size? *Geophys. Res. Lett.* **28**, 17, pp. 3349-3352, 2001.

Izutani Y. and Kanamori, H., Scale-dependence of seismic energy-to-moment ratio for strike-slip earthquakes in Japan. *Geophys. Res. Lett.* **28**, 20, 4007-4010, 2001.

Kanamori, H. and L. Rivera, Static and dynamic scaling relations for earthquakes and their implications fro rupture speed and stress drop, *Bull. Seismol. Soc. Am.* **94**, 314-319, 2004.

Kanamori, H. and Brodsky E. E., The Physics of Earthquakes. *Physics Today, June 2001* pp. 34-40, 2001.

Kanamori, H., Hauksson, E., Hutton L. K., Jones L. M., Determination of earthquake energy release and ML using TERRAscope, *Bull. Seismol. Soc. Am.* **83**, 330-346, 1993.

Kanamori, H. and Heaton, T. H., Microscopic and Macroscopic physics of earthquakes. *In GeoComplexity and Physics of Earthquakes, AGU Geophys. Mono. 120, edited by J. B. Rundle, D. L. Turcotte, and W. Klein, pp 147-163, American Geophysical Union, Washington, D. C.,* 2000.

Kaverina, A., Dreger, D., and Price, E., The combined inversion of seismic and geodetic data fro the source process of the 16 October 1999 Mw 7.1 Hector Mine, California, earthquake, *Bull. Seism. Soc. Am.* **92**, 1266-1280, 2002.

Kikuchi, M. and Fukao, Y., Seismic wave energy inferred from long period body wave inversion. *Bull. Seismol. Soc. Am.* **78**, 1707-1724, 1988.

Kikuchi, M., and Kanamori, H., Inversion of complex body waves-III, *Bull. Seism. Soc. Am.* **81**, 2335-2350, 1991.

Kissling, E. Deep structure of the Alps – what do we really know? *Physics of the Earth and*

Planetary Interiors, **79**, 87-112, 1993.

Malagnini, L., K. Mayeda, A. Akinci, and P.L. Bragato, Estimating absolute site effects, *Bull. Seismol. Soc. Am.*, in press, 2004.

Marchant, R. H., Stampfli, G. M., Subduction of continental crust in the Western Alps. *Tectonophysics* **269**, 217-235, 1997.

Mayeda, K., m_b (L_g coda): A stable single station estimator of magnitude. *Bull. Seismol. Soc. Am.* **83**, 851-861, 1993.

Mayeda, K., Hofstetter A., O'Boyle J. L., Walter, W. R, Stable and transportable regional magnitudes based on coda-derived moment-rate spectra. *Bull. Seismol. Soc. Am.,* **93**, 224-239, 2003.

Mayeda, K., Dreger, D., Walter, W. R., Wurman, G. And Tajima, F. BDSN calibration for Northern California earthquakes from coda-derived source spectra: moment magnitude and radiated energy, *Seism. Res. Lett.,,* **75**, 278, 2004.

Mayeda, K. and Walter W.R., Moment, energy, stress drop, and source spectra of western United States earthquakes from regional coda envelopes. *J. Geophys. Res.* **101**, 11, 195-11,208, 1996.

Morasca, P, Malagnini, L., Akinci, A., Spallarossa, D., Ground-motion scaling in the western Alps. *Bull. Seism. Soc. Am. (submitted),* 2004.

Paul, A., Cattaneo, M., Thouvenot, F., Spallarossa, D.,Béthoux, N., Fréchet, J., A three-dimensional crustal velocity model of the southwestern Alps from local earthquake tomography. *J. Geophis. Res.* **106**, B9, 19,367-19,389, 2001.

Pérez-Campos, X. and Beroza, G. C. An apparent mechanism dependence of radiated seismic energy. *J. Geophys. Res.*. **106**, 11,127-11,136, 2001.

Polino, R., Dal Piaz, G., Grosso, G., Tectonic erosion at the Adria margin and accretionary

processes for the Cretaceous orogeny of the Alps. *Vol. spec. Soc. Geol. It. n°1, pp.345-367,* 1990.

Prejean, S. G. and Ellsworth, W. L., Observations of earthquake source parameters at 2 km depth in the Long Valley caldera, eastern California. *Bull. Seism. Soc. Am.* **91**, 165-177, 2001.

Randall, G. E., Ammon, C. J., Owens, T. J., Moment tensor estimation using regional seismograms from Tibetan Plateau portable network deployment. *Geoph. Res. Lett.* **22**, 1665-1668, 1995.

Rosenbaum, G., Lister G. S., Duboz, C., Relative motions of Africa, Iberia and Europe during Alpine orogeny. *Tectonophysics* **359***, 117-129,* 2002.

Sadigh, K., Chang, C. Y., Egan, J. A., Makdisi, F., Youngs, R. R. Attenuation relationships for shallow crustal earthquakes based on California Strong Motion Data. Seism. Res. Lett. **68,** 1, 154-180, 1997.

Sato, H. and Fehler, M.,. Seismic wave propagation and scattering in the heterogeneous earth. *AIP Press, Modern Acoustic and Signal Processing,* 1998.

Shang, T. and Gao L. S., Transportation theory of multiple scattering and its application to seismic coda waves. *Sci. Sinca, Series B,* **31**, 1503-1514, 1988.

Spallarossa, D., Bindi, D., Augliera, P., Cattaneo, M., An ML scale in Northwestern Italy. *Bull. Seism. Soc. Am., in press,* 2002.

Spudich , P., Joyner, W. B., Lindh, A. G., Boore, D. M., Margaris, B. M., Fletcher, J. B. A revised Ground Motion Prediction Relation for Use in Extensional Tectonic Regimes. Bull. Seism. Soc. Am., **89**, 1156-1170, 1999.

Steidl, J.H., Tumarkin, A.G., and Archuleta, R.J., What is a reference site?, *Bull. Seism. Soc. Am.* **86**, 1733-1748, 1996.

Sue, C., Thouvenot, F., Fréchet, J., and P. Tricart. Earthquake analysis reveals widespread extension in the core of the Western Alps. *J. Geophys. Res.,* **104**, 25611-25622, 1999.

Sue, C. and P. Tricart. Widespread post-nappe normal faulting in the Internal Western Alps: a new constraint on arc dynamics. J. of the Geological Society, **159**, 61-70, 2002.

Sue, C. and P. Tricart. Late alpine brittle extension above the Frontal Pennine thrust near Briançon, France, *Eclogae Geol. Helv.,* 171-181, 1999.

Vassiliou, M. S. and H. Kanamori , The energy release in earthquakes, *Bull. Seism. Soc. Am.* **72**, 371-387, 1982.

Wald, D. J., H. Heaton, Thomas, K. Hudnut, The slip history of the 1994 Northridge, California, earthquake determined from strong-motion, telesismic, GPS, and leveling data. *Bull. Seism. Soc. Am.* **86**, 549-570, 1996.

Wyss M. and Brune J. N., Seismic moment, stress, and source dimensions for earthquakes in the California-Nevada region. *J. Geophys. Res.* **73**, 4681- 4694, 1968.

FIGURE CAPTIONS

Figure 1 - Stations (solid triangles) and events (circles) that were used in this study along with the major tectonic features of the region. CPF: Crustal Penninic Front, the main boundary between external and internal (Penninic) zones; TPB: Tertiary Piemontese Basin.

Figure 2 - Representative narrowband envelopes for the October 31st, 1997 event at station STV2. The strong frequency-dependence in the coda envelopes shape requires that we parameterize as a function of frequency.

Figure 3 – (A) The coda shape parameter γ is plotted as a function of distance for the 4.0-6.0-Hz case. Notice that at short distances γ is large and then decreases with increasing distance. From Equation (2) we see that this parameter controls the shape of the early coda immediately following the direct *S*-wave. (B) The coda shape parameter, *b*, dominates the coda envelope shape at larger times. (C) Peak velocity of the observed coda envelopes is plotted versus distance. In all figures the lines represent the best fitting hyperbola and the parameters for all frequency bands and stations are listed in Table 1.

Figure 4 – To illustrate coda homogeneity and differences with direct *S*-waves, we show examples of two events recorded at stations STV2 and NEGI for two frequency bands, 2.0-3.0-Hz and 20.0-25.0-Hz. (A) Event 972480856 is only 5 km from NEGI and 55 km from STV2. Though the direct waves are decaying as one would expect based upon geometrical spreading and *Q*, the coda envelopes as measured from the origin time have converged to the same level. (B) The reciprocal case for event 990660401 that is 51 km from NEGI and only 8 km from STV2. (C) Example of synthetics, normalized at 120 seconds, were generated at 20 km intervals for the 2.0-3.0-Hz case. (D) Same as 4A, but for the 20.0-25.0-Hz case. These represent our initial assumptions on the spatial distribution of the coda. We then use these to measure raw coda envelope amplitudes by DC shifting the synthetics to match the observed envelopes. We then use a two-station grid-searching technique using Equation 6 to find the best average model for the region using all possible pairs of stations.

Figure 5 –Plots of amplitudes at station STV2 vs. amplitudes at station MONE for two frequency bands, 3.0-4.0-Hz and 10.0-15.0-Hz. The panels on the left show raw,

uncorrected *S* and coda waves along with their associated inter-station standard deviations. The panels on the right are the corresponding distance-corrected amplitudes and here we see that the direct *S*-wave amplitudes are 3-to-4 times more scattered than the coda-derived amplitudes. Notice that the uncorrected coda amplitudes in the left panels also show very little variance, indicating that our initial normalized synthetics (see Figs. 4C and 4D) were very close to the final, best fitting model.

Figure 6 - (A) Distance-corrected coda amplitudes for a range of event sizes that are still in dimensionless units. Using independent moments for the three largest events we can tie the low frequency measurements to an absolute scale. We also use smaller events as empirical Green's function events to derive corrections for the higher frequencies. (B) Example of waveform modelling for seismic moment for one of the larger calibration events. (C) Source spectra in dyne-cm after all corrections for site effect and *S*-to-coda transfer function have been applied.

Figure 7 – (A) $M_{W(coda)}$ from this study is in excellent agreement with M_W derived from a previous study of Morasca *et al.* (2003) using direct *S*-waves. (B) For events greater than M_W ~2.5 we see that $M_{W(coda)}$ scales roughly 1-to-1 with the network M_L, however for smaller events M_W scales with a slope of 2/3 with M_L. This break in slope is expected and is because M_L is being computed below the event's corner frequency where the amplitude is directly proportional to seismic moment. (C) Using the 2.0-3.0-Hz source amplitude from the coda spectra, we have derived our own local magnitude, $M_{L(coda)}$, using Equation 7. A single-station coda measurement can provide the same stability as a network-averaged M_L using direct *S*-waves.

Figure 8 – Using the averaged coda-derived moment-rate spectra, we extrapolated the to f = 0-Hz and $f = \infty$-Hz (assuming an omega-square falloff). We then multiplied by omega, squared the spectra, then integrated to get E_S. Solid diamonds represent events where the extrapolated *S*-wave energy was less than 30% of the total and the circles represent events where we extrapolated 30-to-45% of the energy. In both cases we see a good correspondence between energy estimates from the western United States (Mayeda *et al.*, 1996) and the Cajon Pass borehole (Abercrombie, 1995)which shows a clear increase in apparent stress with increasing magnitude. For the larger events in our study ($M_w > \sim 3.5$), we observe a systematic increase in energy perhaps reflecting a higher state of stress in this region relative to the western U.S. results.

Table 1: Calibration parameters for velocity, coda shape, and path corrections used for all stations. v_0, v_1, v_2, are the parameters used in the hyperbola (Eq. 3) describing group velocity of the peak *S*-wave arrival; b_0, b_1, b_2 and γ_0, γ_1, γ_2 are the coda envelope shape parameters used in the hyperbola (Eq. 4) and (Eq. 5) respectively; p_1 and p_2 are the path parameters from Equation (6).

Freq. Hz	v_0	v_1	v_2	b_0	b_1	b_2	γ_0	γ_1	γ_2	p_1	p_2
0.3-0.5	2.65	6	4	-0.0032	0.00	10-4	0.1	0	1	0.75	100
0.5-0.7	2.75	8	4	-0.0047	0.14	143	0.1	-13	7	3.50	300
0.7-1.0	2.85	8	4	-0.0058	0.18	500	0.1	-35	34	1.50	200
1.0-1.5	3.00	4	4	-0.0073	0.10	500	0.1	-25	17	2.25	200
1.5-2.0	3.05	2	1	-0.0145	0.00	10-4	0.1	-31	19	2.50	150
2.0-3.0	3.15	2	1	-0.0131	0.00	10-4	0.1	64	101	1.25	50
3.0-4.0	3.15	2	1	-0.0151	0.06	500	0.1	-51	52	2.00	100
4.0-6.0	3.15	2	1	-0.0162	0.02	2	0.1	-62	75	2.25	100
6.0-8.0	3.20	2	1	-0.0209	0.14	487	0.1	-41	45	1.75	50
8.0-10.0	3.15	2	1	-0.0115	4.00	484	0.4	-9	6	3.00	100
10.0-15.0	3.20	2	1	-0.0115	1.06	53	0.6	0	2.4	4.25	150
15.0-20.0	3.15	2	1	-0.0115	3.26	163	0.5	0	1.9	2.25	100
20.0-25.0	3.15	2	1	-0.0230	0.68	68	0.4	0	1.4	1.50	50

Table 2: Site and *S*-to-coda transfer function corrections for GENL, MONE, NEGI, STV2 and TRAV. We note that for a given frequency band, the variation between stations represents the relative site response.

Freq. Hz	GENL	MONE	NEGI	STV2	TRAV
0.3-0.5	20.2231	20.2595	20.0143	20.4184	20.4709
0.5-0.7	21.2562	20.2595	21.1804	21.4607	21.4134
0.7-1.0	20.1421	20.2443	20.0583	20.3967	20.2928
1.0-1.5	19.7647	19.8311	19.7819	20.0358	19.8568
1.5-2.0	20.5172	20.5181	20.5032	20.7069	20.5903
2.0-3.0	19.5517	19.2838	19.4993	19.6804	19.4817
3.0-4.0	19.9319	19.4793	19.8276	20.0450	19.7869
4.0-6.0	19.9240	19.5344	19.8898	20.0932	19.8963
6.0-8.0	20.1220	19.5848	19.9790	20.1852	20.0684
8.0-10.0	20.3995	19.7861	20.1634	20.3681	20.2344
10.0-15.0	20.5252	20.3450	20.2612	20.5109	20.2771
15.0-20.0	21.1161	20.8756	20.7326	20.8510	20.6148
20.0-25.0	21.0222	21.1060	20.9756	20.9646	20.9160

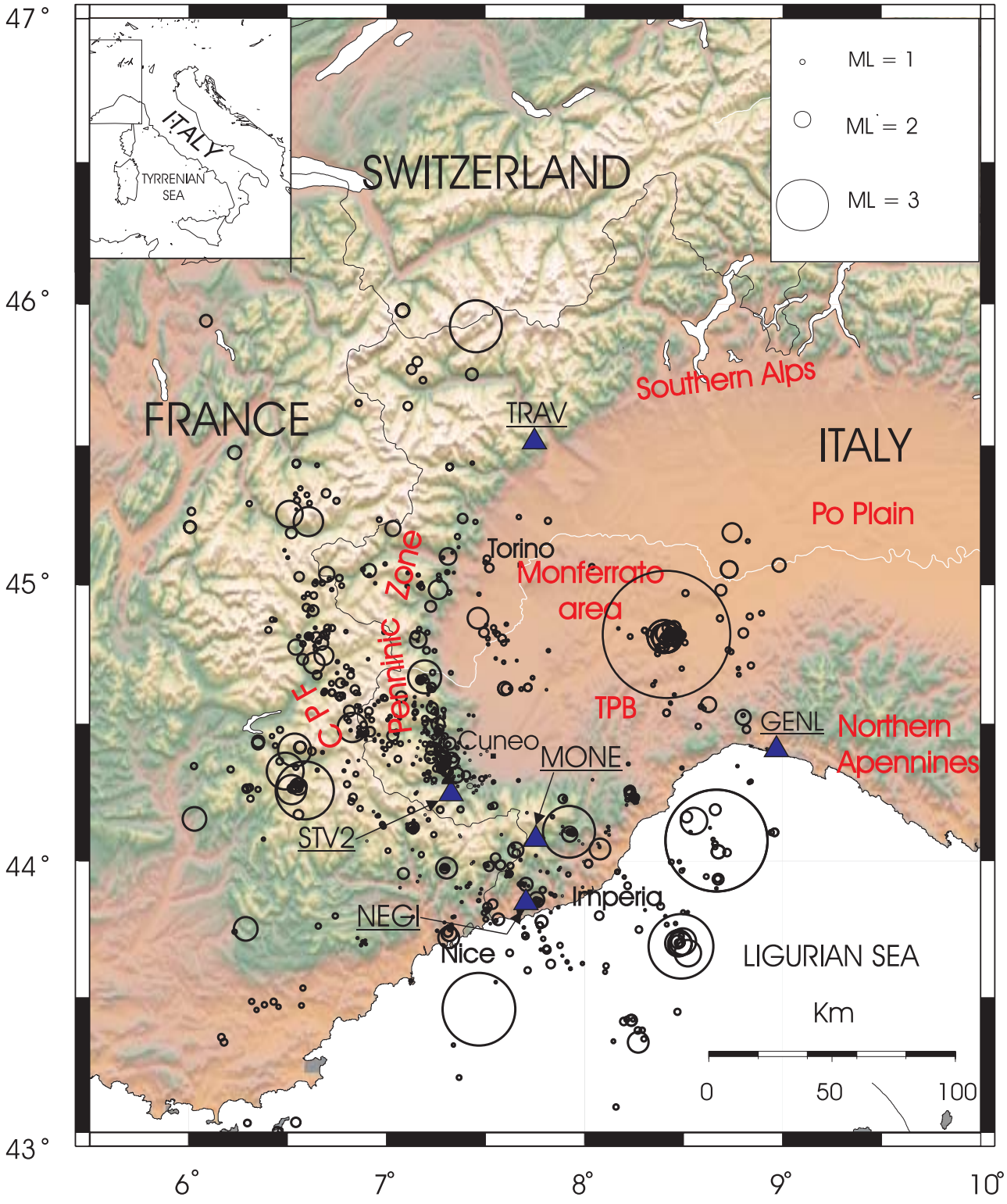
47°
46°
45°
44°
43°
6°
7°
8°
9°
10°
ITALY
TYRRENIAN SEA
SWITZERLAND
FRANCE
ITALY
ML = 1
ML = 2
ML = 3
Southern Alps
Po Plain
TRAV
Torino
Monferrato area
CPF
Pennine Zone
TPB
GENL
Northern Apennines
Cuneo
MONE
STV2
Imperia
NEGI
Nice
LIGURIAN SEA
Km
0
50
100

Figure 1

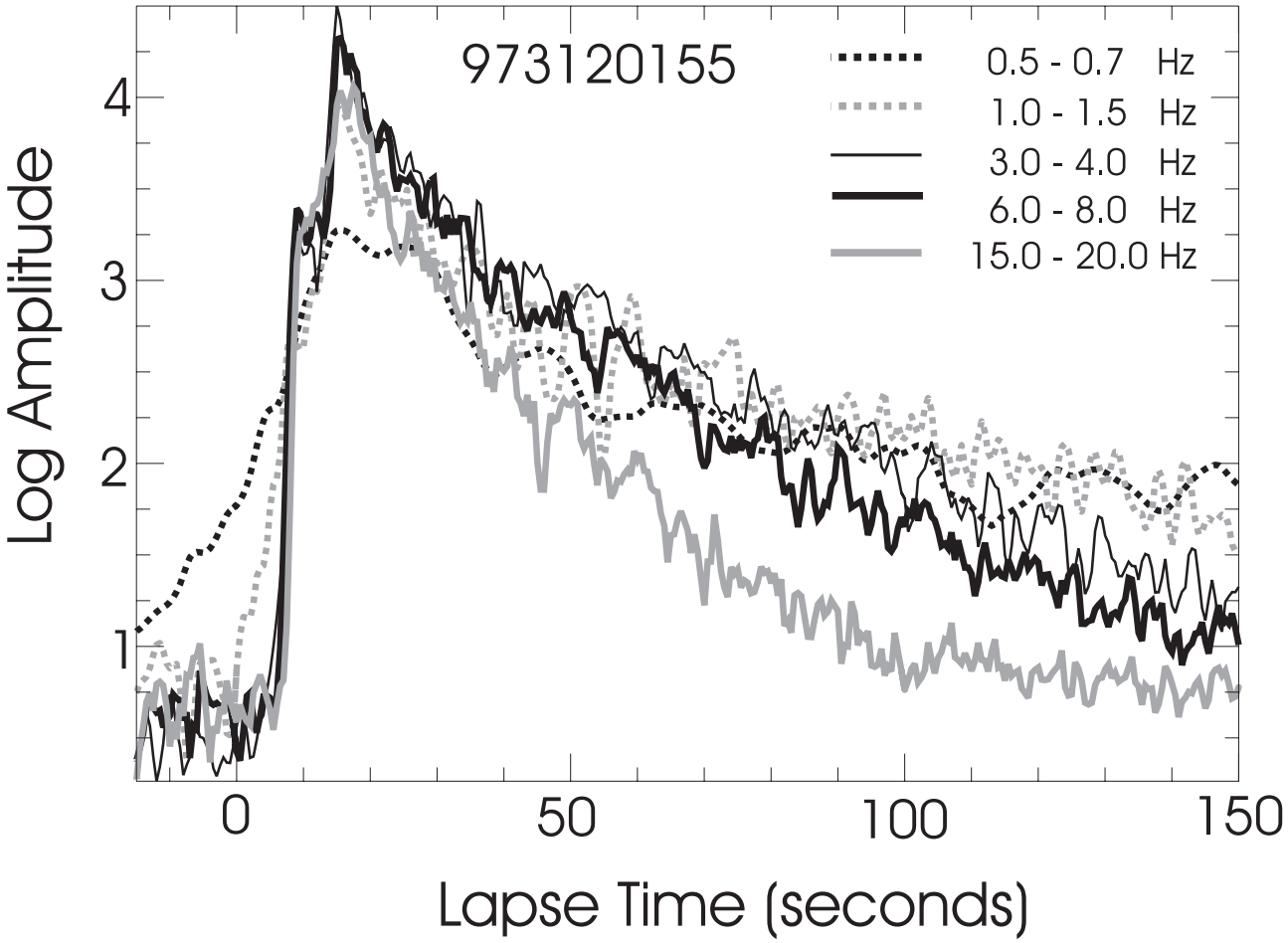
973120155
0.5 - 0.7 Hz
1.0 - 1.5 Hz
3.0 - 4.0 Hz
6.0 - 8.0 Hz
15.0 - 20.0 Hz
Log Amplitude
1
2
3
4
0
50
100
150
Lapse Time (seconds)

Figure 2

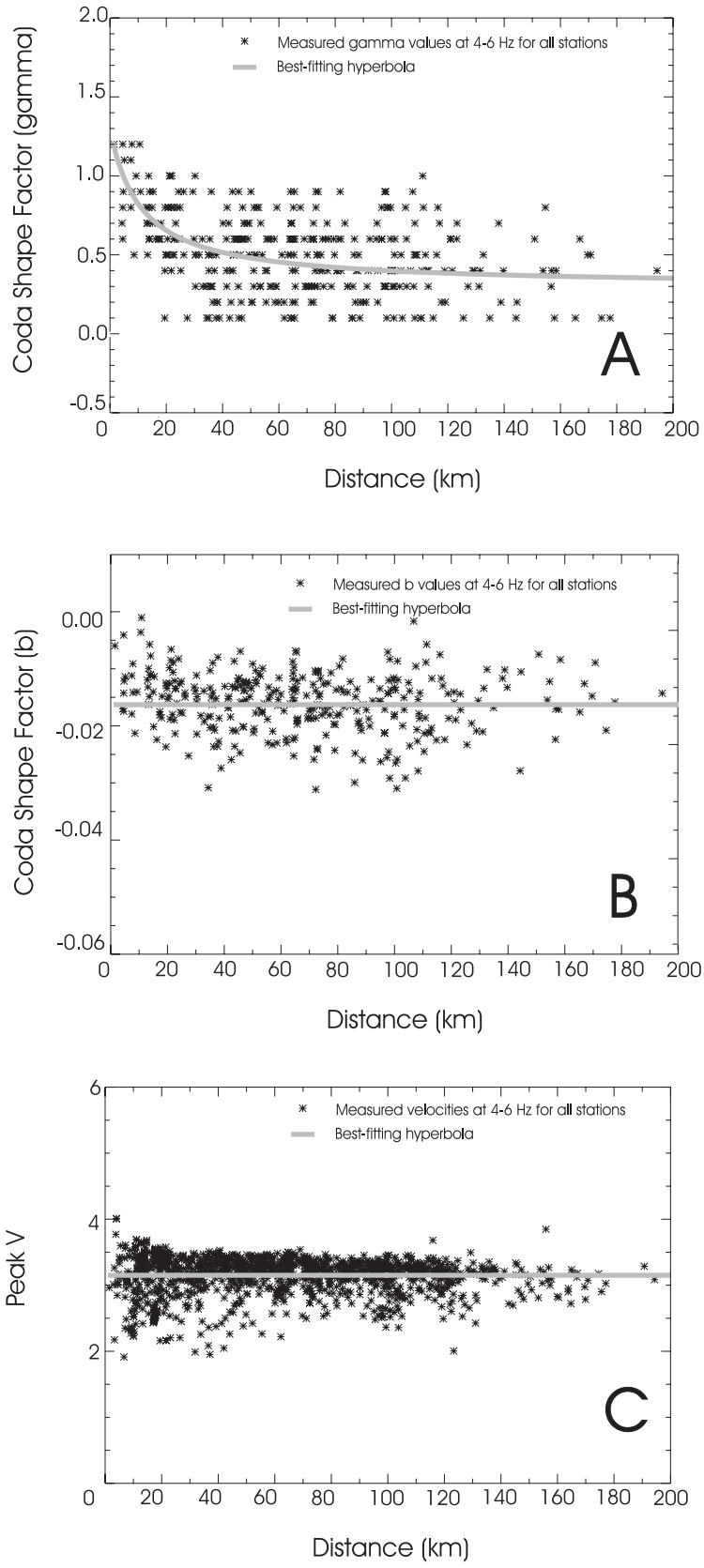
Measured gamma values at 4-6 Hz for all stations
Best-fitting hyperbola
Coda Shape Factor (gamma)
2.0
1.5
1.0
0.5
0.0
-0.5
0
20
40
60
80
100
120
140
160
180
200
Distance (km)
A
Measured b values at 4-6 Hz for all stations
Best-fitting hyperbola
Coda Shape Factor (b)
0.00
-0.02
-0.04
-0.06
Distance (km)
B
Measured velocities at 4-6 Hz for all stations
Best-fitting hyperbola
Peak V
6
4
2
Distance (km)
C

Figure 3

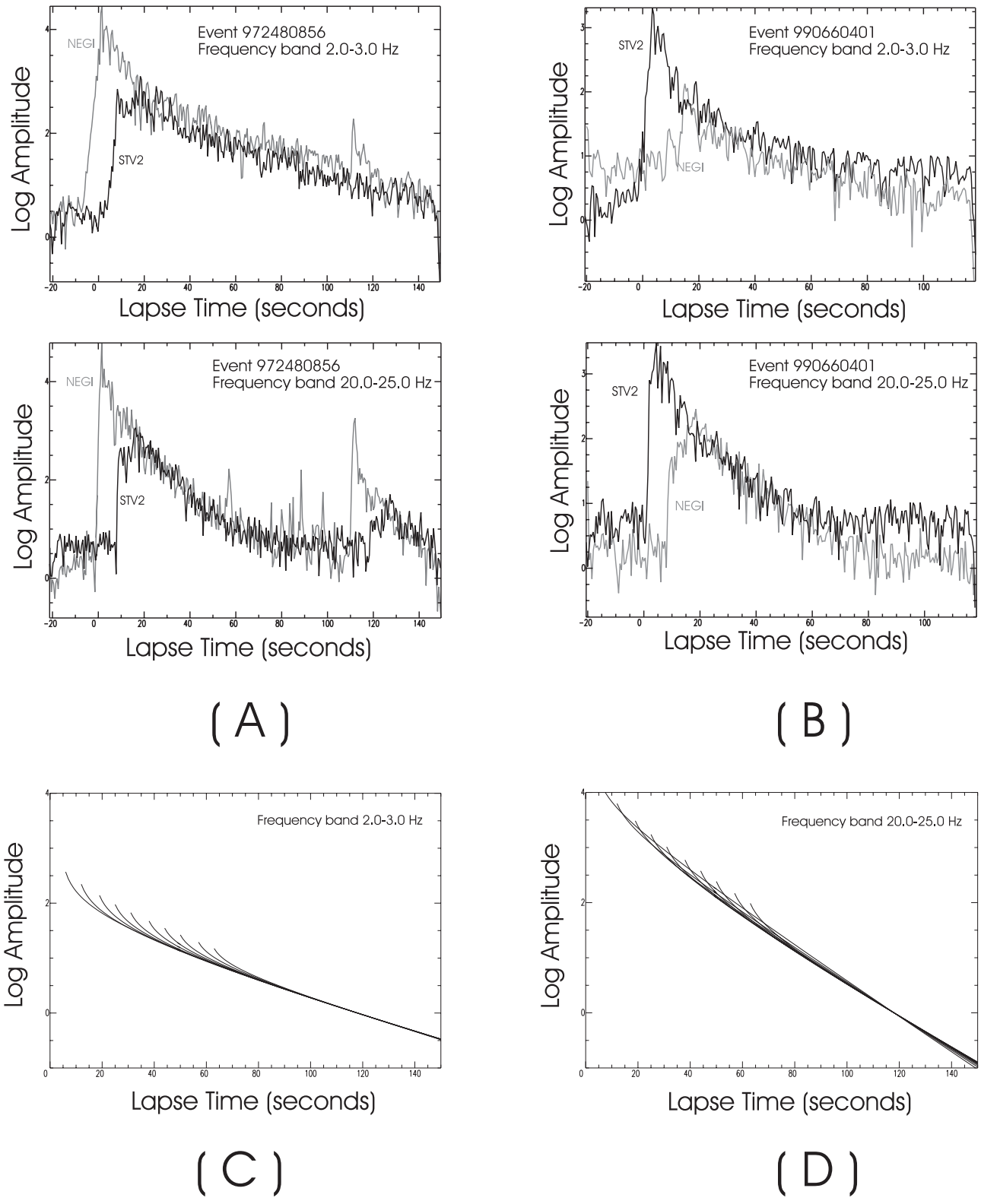
Event 972480856
Frequency band 2.0-3.0 Hz
NEGI
STV2
Log Amplitude
Lapse Time (seconds)
Event 990660401
Frequency band 2.0-3.0 Hz
STV2
NEGI
Log Amplitude
Lapse Time (seconds)
Event 972480856
Frequency band 20.0-25.0 Hz
NEGI
STV2
Log Amplitude
Lapse Time (seconds)
Event 990660401
Frequency band 20.0-25.0 Hz
STV2
NEGI
Log Amplitude
Lapse Time (seconds)
(A)
(B)
Frequency band 2.0-3.0 Hz
Log Amplitude
Lapse Time (seconds)
Frequency band 20.0-25.0 Hz
Log Amplitude
Lapse Time (seconds)
(C)
(D)

Figure 4

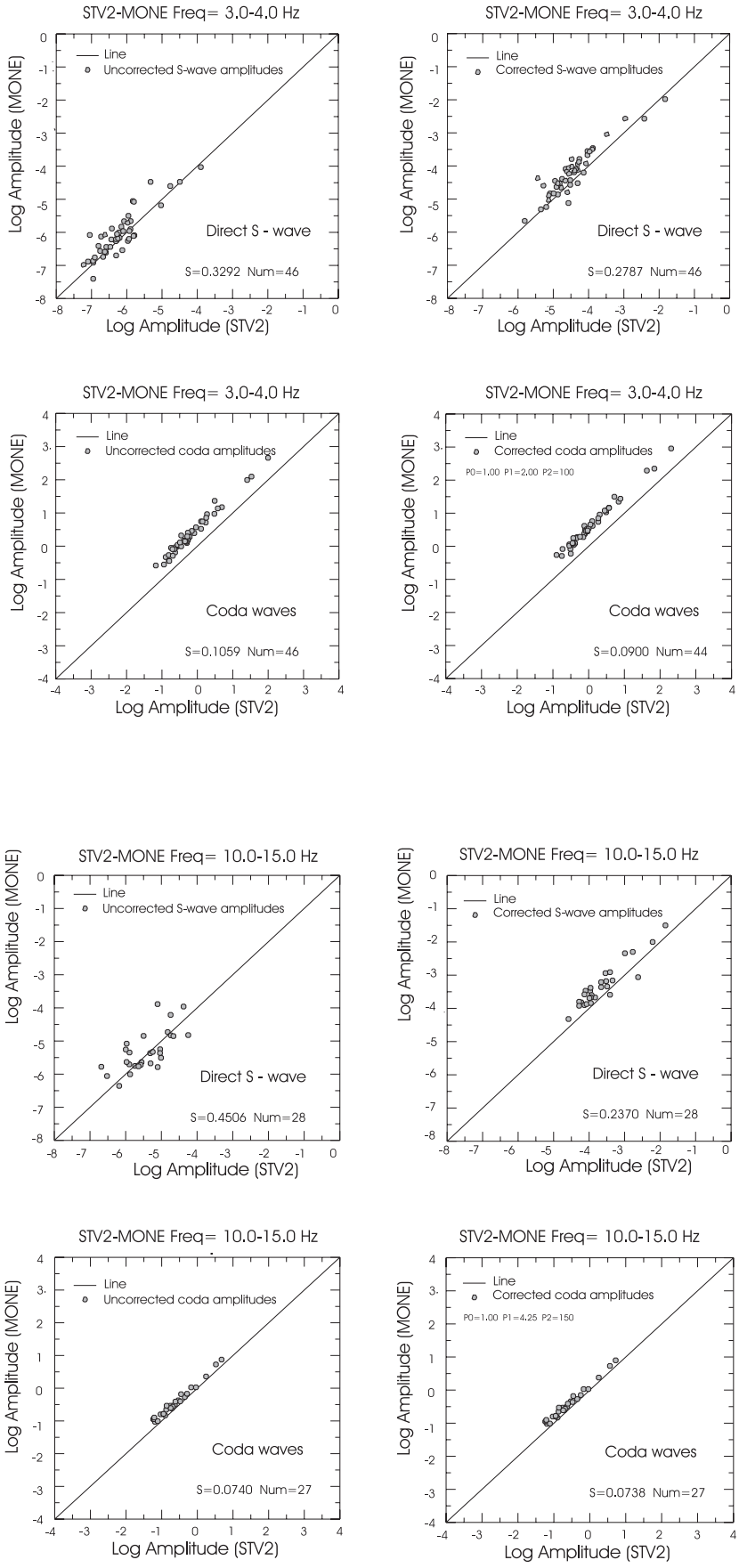
STV2-MONE Freq= 3.0-4.0 Hz
Line
Uncorrected S-wave amplitudes
Direct S - wave
S=0.3292 Num=46
Log Amplitude (MONE)
Log Amplitude (STV2)
STV2-MONE Freq= 3.0-4.0 Hz
Line
Corrected S-wave amplitudes
Direct S - wave
S=0.2787 Num=46
Log Amplitude (MONE)
Log Amplitude (STV2)
STV2-MONE Freq= 3.0-4.0 Hz
Line
Uncorrected coda amplitudes
Coda waves
S=0.1059 Num=46
Log Amplitude (MONE)
Log Amplitude (STV2)
STV2-MONE Freq= 3.0-4.0 Hz
Line
Corrected coda amplitudes
P0=1.00 P1=2.00 P2=100
Coda waves
S=0.0900 Num=44
Log Amplitude (MONE)
Log Amplitude (STV2)
STV2-MONE Freq= 10.0-15.0 Hz
Line
Uncorrected S-wave amplitudes
Direct S - wave
S=0.4506 Num=28
Log Amplitude (MONE)
Log Amplitude (STV2)
STV2-MONE Freq= 10.0-15.0 Hz
Line
Corrected S-wave amplitudes
Direct S - wave
S=0.2370 Num=28
Log Amplitude (MONE)
Log Amplitude (STV2)
STV2-MONE Freq= 10.0-15.0 Hz
Line
Uncorrected coda amplitudes
Coda waves
S=0.0740 Num=27
Log Amplitude (MONE)
Log Amplitude (STV2)
STV2-MONE Freq= 10.0-15.0 Hz
Line
Corrected coda amplitudes
P0=1.00 P1=4.25 P2=150
Coda waves
S=0.0738 Num=27
Log Amplitude (MONE)
Log Amplitude (STV2)

Figure 5

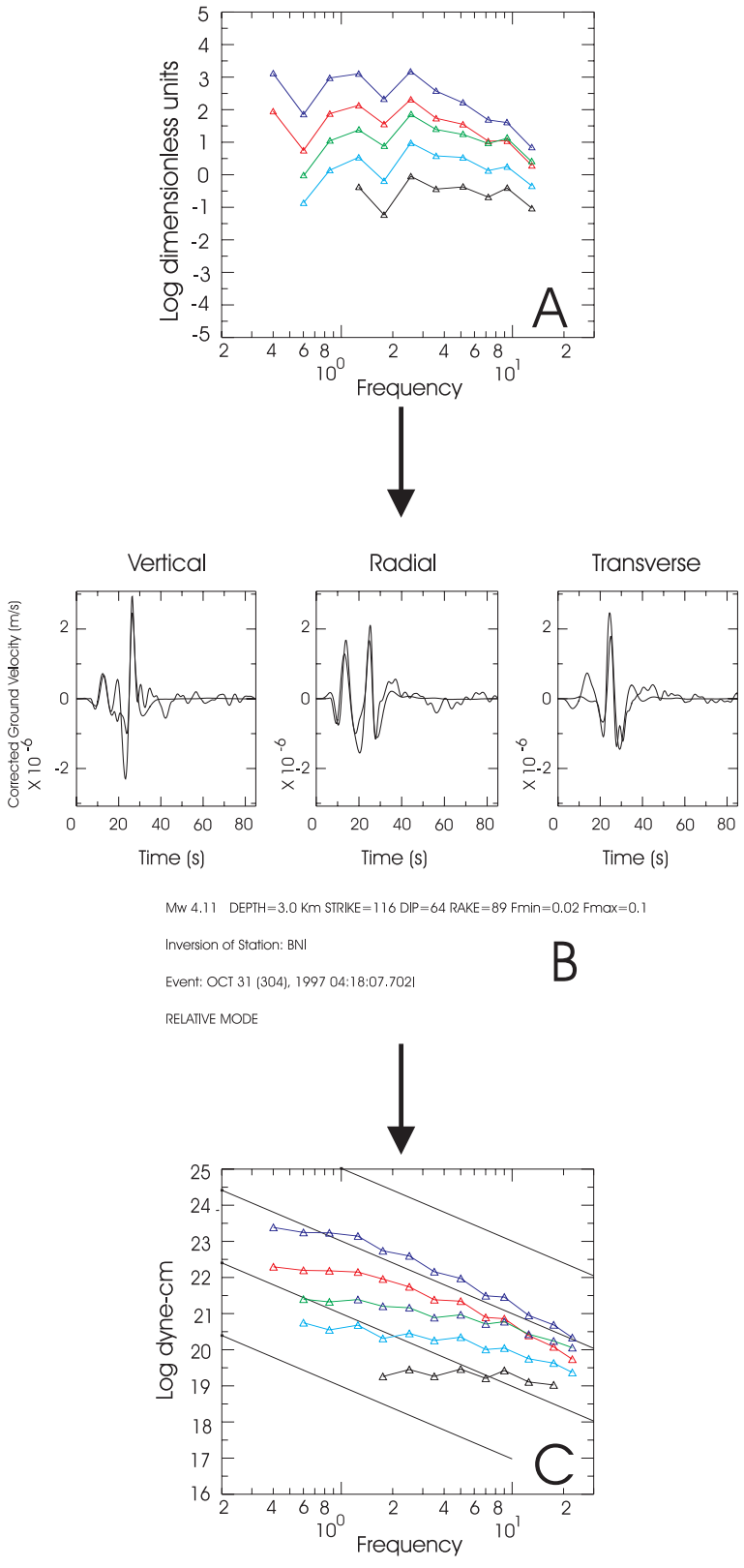
Log dimensionless units
Frequency
A
Vertical
Radial
Transverse
Corrected Ground Velocity (m/s)
X 10 -6
Time (s)
Mw 4.11 DEPTH=3.0 Km STRIKE=116 DIP=64 RAKE=89 Fmin=0.02 Fmax=0.1
Inversion of Station: BNI
Event: OCT 31 (304), 1997 04:18:07.702I
RELATIVE MODE
B
Log dyne-cm
Frequency
C

Figure 6

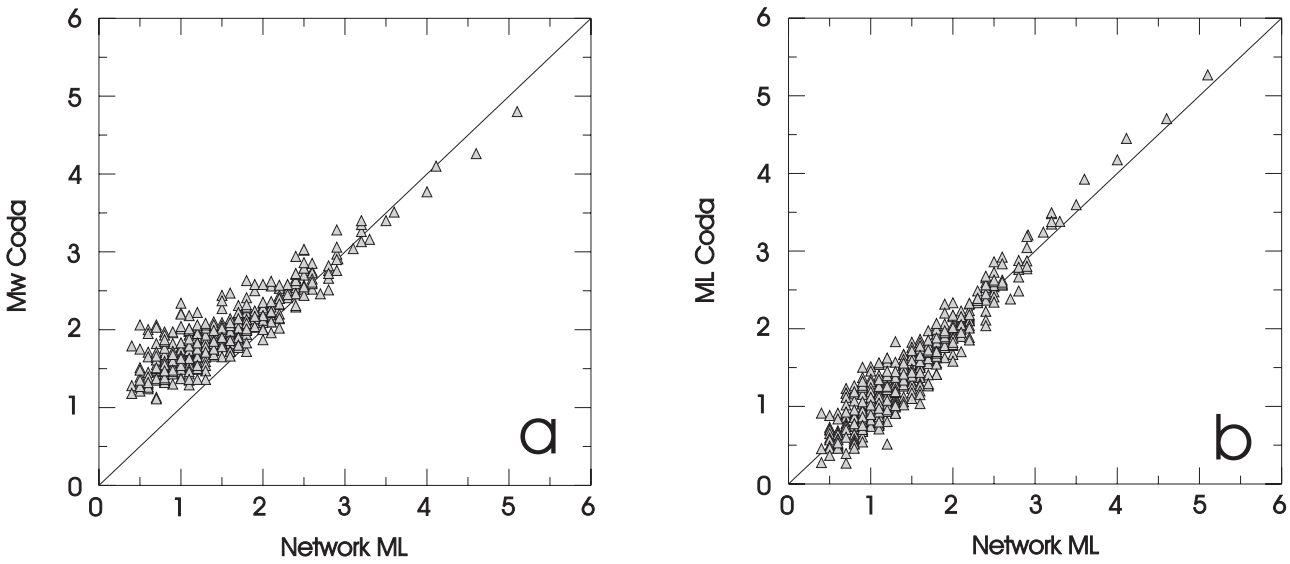

Figure 7

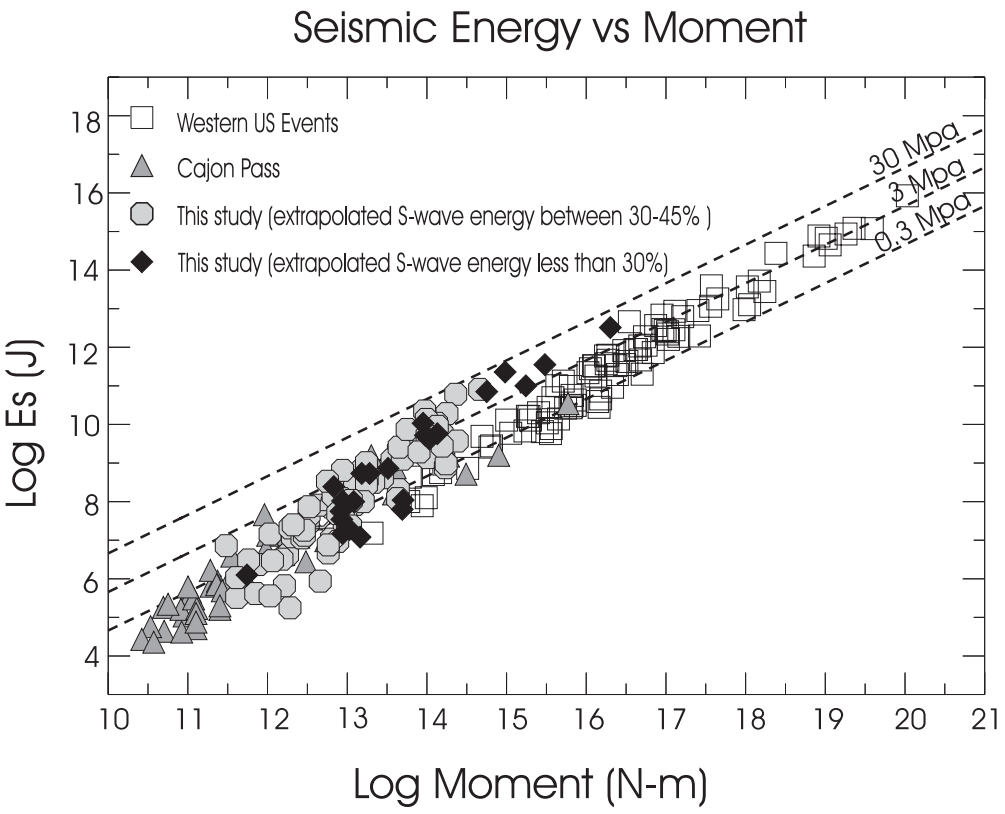
Seismic Energy vs Moment
Western US Events
Cajon Pass
This study (extrapolated S-wave energy between 30-45%)
This study (extrapolated S-wave energy less than 30%)
30 Mpa
3 Mpa
0.3 Mpa
Log Es (J)
Log Moment (N-m)
18
16
14
12
10
8
6
4
10
11
12
13
14
15
16
17
18
19
20
21

Figure 8

University of California
Lawrence Livermore National Laboratory
Technical Information Department
Livermore, CA 94551